Nano Research

Open Access

Research Article

Design synthesis and synergistic anticorrosion performance of ZIF-8/NiAl LDH heterojunction nanocontainers

Yuan Ma[1], Tong Li[1], Si-Rui Zhao[1], Zhou-Tao Feng[1], and Jin-Ku Liu[1,2] ✉

[1] *Key Laboratory for Advanced Materials, School of Chemistry and Molecular Engineering, East China University of Science and Technology, Shanghai 200237, China*
[2] *Material Corrosion and Protection Key Laboratory of Sichuan province, Zigong 643000, China*

Cite this article: *Nano Research*, **2025**, *18*, 94907000. https://doi.org/10.26599/NR.2025.94907000

ABSTRACT: This study introduces a novel relay and synergistic anti-corrosion mechanisms by constructing an active anticorrosive coating with nanocontainers through the combination of zinc-based zeolitic imidazolate framework materials (ZIF-8) and layered double hydroxides loaded with molybdate anions (MoO_4^{2-} LDHs). The incorporation of ZIF-8 provided the material with abundant surface nano-micropores, enhancing its adsorption capacity for corrosive ions such as OH^- and Cl^-. Simultaneously, this adsorption enabled the ZIF-8-loaded NiAl-MoO_4^{2-} LDH to receive signals induced by Cl^- stimulation or pH changes. After receiving the signals, the corrosion inhibitor MoO_4^{2-} encapsulated within the NiAl-MoO_4^{2-} LDH was released responsively and exchanged with Cl^-. The released MoO_4^{2-} from nanocontainers adsorbed onto localized corrosion sites, forming a passivation film, thereby blocking the diffusion path of Cl^-. Additionally, this study demonstrated that the self-assembly of ZIF-8 effectively reduced the hydrophilicity of LDH and enhanced the resistance of coating to permeability. Through supramolecular interactions between LDH hydroxyl groups, metal-organic framework (MOF) functional groups and organic epoxy resin, the cross-linking of the coating and the interfacial compatibility of the materials were significantly improved. The Z-type heterojunction composed of nickel-based LDH and metal organic frameworks not only increased the specific surface area and capacitance performance but also provided photo-induced cathodic protection for metal substrates with matched bandgaps. The experimental results showed that the impedance properties of the ZIF-8/NiAl-MoO_4^{2-} LDH coatings were 28.43 times of pure epoxy after 168 h. This work can provide new insights and assistance for the study of anti-corrosion mechanisms.

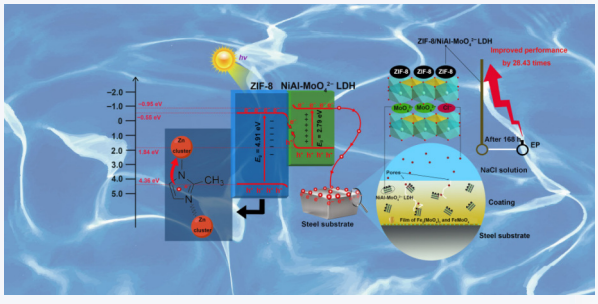

KEYWORDS: nanocontainers, synergistic mechanisms, anti-corrison, layered double hydroxide (LDH), zeolitic imidazolate framework-8 (ZIF-8)

1 Introduction

Metal corrosion is a prevalent issue leading to numerous accidents, resource wastage and heavy metal pollution annually. In the realm of metal surface corrosion protection, organic coatings are extensively employed due to their cost-effectiveness and functional adaptability [1]. However, they suffer from certain limitations such as susceptibility to external mechanical damage, ultraviolet (UV) degradation of polymerized chains and the occurrence of random defects during the curing process, all of which contribute to a reduction in their service life. Consequently, there has been widespread research into the development of functional anti-corrosion fillers for use in organic coatings aimed at steel protection [2, 3]. Functional nanomaterials are often incorporated as corrosion-inhibiting agents dispersed within organic coatings to address the various defects that arise during the curing process. They play a multifunctional role in active corrosion inhibition, passive barrier formation and enhancement of mechanical properties, thus broadening the anti-corrosion capabilities of organic coatings.

Oxygenate-containing materials of the VIB group element Mo are considered a safe and green alternative to chromium(VI)-containing corrosion protection materials, which can serve as functional materials providing effective corrosion inhibition for metal substrates [4]. Yasakau incorporated amorphous cerium molybdate nanowires into resin coatings, where $Ce(MoO_4)_2$ nanowires filled micro-sized defects of the coating [5]. These

Received: June 30, 2024; **Revised:** August 13, 2024
Accepted: August 24, 2024

✉Address correspondence to jkliu@ecust.edu.cn

nanowires decomposed upon exposure to corrosive solutions, releasing Ce^{4+} and MoO_4^{2-} ions to passively protect aluminum alloys. However, direct incorporation of such inorganic molybdate nanomaterials into organic coatings poses challenges related to interfacial compatibility and agglomeration, thereby compromising long-lasting protection. Hence, the use of stabilized nanocontainers for MoO_4^{2-} storage emerges as a promising approach to enhance molybdate compatibility with organic coatings and prolong protective properties. Abrantes Leal, D. developed zinc-containing nanocontainers for storing molybdate corrosion inhibitors in epoxy (EP) coatings [6], aiming to achieve precise corrosion inhibition protection of carbon steel substrates in areas prone to pitting corrosion or coating damage induced by corrosive environments affecting MoO_4^{2-} release. Layered double hydroxide (LDH) materials are widely utilized in catalysis, adsorption and corrosion prevention due to their unique optoelectronic properties and diverse functionalities [7–10]. LDH materials, characterized by a dense layered structure effectively impeding corrosive media penetration and main layers of LDH are linked by intermolecular forces and by modifying synthesis conditions, a tunable unique interlayer structure can be achieved, forming corridors between main layers capable of substance adsorption or anion loading [11–13]. Thus, LDHs are considered suitable nanocontainers for MoO_4^{2-} accommodation to enhance corrosion inhibitor compatibility. However, as superhydrophilic materials, LDHs are prone to coating wetting by corrosive media, leading to accelerated coating penetration and loss of protective capability [14]. Additionally, two-dimensional LDH nanomaterials in epoxy resins exhibit insufficient coating density enhancement. Therefore, composite modification of LDH materials to enhance multiple types of corrosion protection, weaken hydrophilicity and improve densification as coating fillers is of significant interest. The present work is designed to form a protective composite passivation film by adsorption of MoO_4^{2-} that is released during the corrosion response on the localized corrosion sites on the surface of S45C carbon steel, to further prevent the adsorption of Cl^- on the metal surface and the corrosion response [15, 16].

Forming a heterostructure with two materials possessing matched energy bands effectively promotes photogenerated carrier separation and enhances carrier transport efficiency, thus realizing Photocathodic protection [17–20]. Liu prepared type II heterojunction photoanode materials of UIO-66-NH_2 modified TiO_2 [21], transferring photoelectrons from the organic ligand to the metal body with the TiO_2 conduction band (CB), ultimately reaching the metal surface. This reduced charge transfer impedance compared to single-component TiO_2 photoanodes, significantly increasing photogenerated current density and providing a more negative and stable polarization potential for the alloy. Zeolitic imidazolate framework (ZIF), known for its stability, high specific surface area and organic functionalities, coupled with its nano-porous structure conferring excellent hydrophobicity and adsorption capacity, presents an opportunity for developing smart coatings with active protection and good interfacial compatibility [22–25]. For instance, Huang grew benzotriazole (BTA)-ZIF-8 nanocontainers *in situ* on hydroxylated h-BN nanosheets (BN-OH) to achieve active inhibition through the release of built-in BTA triggered by ZIF-8 [26]. Additionally, the "labyrinth effect" of the nanosheets improved interfacial compatibility with the coating substrate, resulting in excellent passive barrier properties. Furthermore, combining ZIF-8 with the upper hydroxyl group, with the surface N–H acting as a co-curing agent, synergistically participated in the epoxy resin ring-opening curing process, addressing the issue of insufficient densification of epoxy coatings. This heterojunction formation between ZIF-8 and epoxy resin provides a variety of protective functions for the coating.

The ZIF-8/NiAl-MoO_4^{2-} LDH heterojunction nanocontainers were synthesized. The loaded MoO_4^{2-} was actively released under the stimulation of corrosive medium, reducing the anodic reactivity of the corroded sites on the metal surface. Additionally, the composite ZIF-8 synergistically enhanced the release and protection efficiency of MoO_4^{2-}. Interlayer corridors of nanocontainers acted as ion traps, precisely capturing Cl^- penetrating into the coating, thus reducing the potential for sustained corrosion. ZIF-8 formed a heterojunction with NiAl LDH via surface self-assembly and the intercalation of MoO_4^{2-} increased the interlayer spacing, improving the internal charge transfer ability of the material and further enhancing photoprotection. Furthermore, compounding ZIF-8 reduced the hydrophilicity of LDH and improved interfacial compatibility with organic materials. This work designed and synthesized self-supported structural nano-heterojunction containers of corrosion inhibitors ZIF-8/NiAl-MoO_4^{2-} LDH, enhancing composite compatibility, molybdate corrosion protection ability and active corrosion inhibition and synergistic protection. These findings provide an important reference for designing new anticorrosive materials with synergistic corrosion protection.

2 Experimental section

2.1 Experimental material

Aluminum nitrate hydrate ($Al(NO_3)_3{\cdot}9H_2O$), sodium chloride (NaCl) and anhydrous methanol (CH_3OH) were provided by Sinopharm Chemical Reagent Co., Ltd. 2-Methylimidazole ($C_4H_6N_2$), nickel nitrate hexahydrate ($Ni(NO_3)_2{\cdot}6H_2O$), ammonium molybdate heptahydrate ($(NH_4)_6Mo_7O_{24}{\cdot}4H_2O$)) and urea ($CO(NH_2)_2$) were purchased from Shanghai Macklin Biochemical Co., Ltd. Zinc nitrate hexahydrate ($Zn(NO_3)_2{\cdot}6H_2O$), sodium sulfate (Na_2SO_4), sodium hydroxide (NaOH) were purchased from Shanghai Aladdin Biochemical Technology Co., Ltd. Ammonium fluoride (NH_4F), Nafion 117 membrane solution was purchased from Sigma-Aldrich (Shanghai) Trading Co., Ltd. The epoxy resin used was HL-001 and the solvents used in the experiments included ultrapure water and anhydrous methanol.

2.2 Material synthesis

2.2.1 *Synthesis of NiAl-NO_3^- LDH*

50 mL of a mixture of 6 mmol $Ni(NO_3)_2$ and 2 mmol $Al(NO_3)_3$ and 50 mL of 0.5 mol·L^{-1} NaOH solution were configured. Under conditions of magnetic stirring, a prepared mixture and a NaOH solution were incrementally introduced into 50 mL of ultrapure water. The pH of the solution was rigorously regulated within the range of pH = 9.0 ± 0.1 throughout the duration of the procedure. The suspension was subsequently transferred to a 200 mL hydrothermal kettle equipped with a polytetrafluoroethylene (PTFE) liner and subjected to an aging process at 120 °C for a duration of 24 h. Upon completion, the resulting product was recovered, filtered and subjected to three consecutive washes with ultrapure water. Subsequently, it underwent drying in a vacuum

oven maintained at 60 °C for a period of 12 h. The resultant material was named as NiAl-NO_3^- LDH

$$Ni^{2+} + 2OH^- \rightarrow Ni(OH)_2 \quad (1)$$

$$Al^{3+} + 3OH^- \rightarrow Al(OH)_3 \quad (2)$$

$$(1-x)Ni(OH)_2 + xAl(OH)_3 \rightarrow [Ni_{1-x}Al_x(OH)_2]^{x+}(NO_3^-)_x \cdot mH_2O \quad (3)$$

2.2.2 Synthesis of NiAl-CO_3^{2-} LDH and NiAl-MoO_4^{2-} LDH

100 mL of a solution containing 6 mmol $Ni(NO_3)_2$, 2 mmol $Al(NO_3)_3$, 0.2 mmol NH_4F mixed with 48 mmol $CO(NH_2)_2$ was prepared. The suspension was subsequently transferred to a 200 mL hydrothermal kettle equipped with a PTFE liner and subjected to an aging process at 120 °C for a duration of 24 h. Upon completion, the resulting product was recovered, filtered and subjected to three consecutive washes with ultrapure water. Subsequently, it underwent drying in a vacuum oven maintained at 60 °C for 12 h. The resulting product was named NiAl-CO_3^{2-} LDH

$$CO(NH_2)_2 + 3H_2O \rightarrow NH_4^+ + CO_2 + 2OH^- \quad (4)$$

$$CO_2 + 2OH^- \rightarrow CO_3^{2-} + H_2O \quad (5)$$

$$(1-x)Ni(OH)_2 + xAl(OH)_3 \rightarrow [Ni_{1-x}Al_x(OH)_2]^{x+}(CO_3^{2-})_{x/2} \cdot mH_2O \quad (6)$$

100 mL of a mixed solution containing 6 mmol $Ni(NO_3)_2$, 2 mmol $Al(NO_3)_3$, 0.5 mmol $(NH_4)_6Mo_7O_{24}$, 0.2 mmol NH_4F with 56 mmol $CO(NH_2)_2$ was prepared. The suspension was subsequently transferred to a 200 mL hydrothermal kettle equipped with a PTFE liner and subjected to an aging process at 120 °C for a duration of 24 h. Upon completion, the resulting product was recovered, filtered and subjected to three consecutive washes with ultrapure water. Subsequently, it underwent drying in a vacuum oven maintained at 60 °C for 12 h. The resulting product was named NiAl-MoO_4^{2-} LDH

$$(NH_4)_6Mo_7O_{24} + 8OH^- \rightarrow 6NH_4^+ + 7MoO_4^{2-} + 4H_2O \quad (7)$$

$$(1-x)Ni(OH)_2 + xAl(OH)_3 \rightarrow [Ni_{1-x}Al_x(OH)_2]^{x+}(MoO_4^{2-})_{x/2} \cdot mH_2O \quad (8)$$

2.2.3 Synthesis of ZIF-8/NiAl-CO_3^{2-} LDH and ZIF-8/NiAl-MoO_4^{2-} LDH materials

The prepared NiAl-CO_3^{2-} LDH and NiAl-MoO_4^{2-} LDH materials were ultrasonically dispersed in 40 mL of ethanol solution containing 3 mmol of $Zn(NO_3)_2$ and 40 mL of ethanol solution containing 18 mmol of 2-methylimidazole was added dropwise to the suspension and magnetically stirred and aged for 24 h at room temperature to fully carry out the reaction. Subsequently, the products were collected by centrifugation and filtered, washed three times with anhydrous ethanol and ultrapure water and dried in a vacuum oven at 60 °C for 12 h. The resulting products were named ZIF-8/NiAl-CO_3^{2-} LDH and ZIF-8/NiAl-MoO_4^{2-} LDH

$$Zn^{2+} + 2C_4H_6N_2 + NiAl - CO_3^{2-}LDH \rightarrow C_8H_{12}N_4Zn(ZIF-8)/NiAl - CO_3^{2-}LDH \quad (9)$$

$$Zn^{2+} + 2C_4H_6N_2 + NiAl - MoO_4^{2-}LDH \rightarrow C_8H_{12}N_4Zn(ZIF-8)/NiAl - MoO_4^{2-}LDH \quad (10)$$

2.3 Epoxy coating preparation

0.8 g of the five prepared NiAl LDH with ZIF-8/NiAl LDH comprising the composite coatings were added to 8.0 g of epoxy resin, respectively and then magnetically stirred for 4 h to ensure homogeneous dispersion. 2.0 g of curing agent was added and the coatings were pre-cured for 30 min under stirring conditions. After sanding the substrate with sandpaper in the order of 180, 360 and 600 mesh, it was cleaned and degreased with anhydrous ethanol. S45C steel coated with pure EP coating was prepared as a control. The coated steel plates were cured and dried at room temperature (~ 20 °C) for 7 days. All steel surfaces were left intact for electrochemical testing.

2.4 Characterizations sections

The crystalline phase and chemical bonding composition were analyzed by powder X-ray diffraction (XRD, Rigaku, Ultima IV, Cu K-radiation) in conjunction with Fourier transform infrared spectrometer (FT-IR, Shimadzu, IRPrestige-21). The elemental chemical composition of the material surface was characterized by X-ray photoelectron spectroscopy (XPS, Thermo Scientific, Thermo ESCALAB 250Xi). The quantitative analysis of the elemental content of the sample was determined through inductively coupled plasma optical emission spectrometry (ICP-OES, Agilent ICP-OES 725). The material's thermal stability was analyzed using thermogravimetric (TG) analyzer (Netzsch, STA 449 F5). The specific surface area, adsorption and desorption profiles and pore size distribution were characterized by the Brunner–Emmett–Taylor method (BET, JW-BK100C) in an N_2 atmosphere at 77 K. The UV–visible diffuse reflectance spectroscopy (UV–Vis DRS, Shimadzu UV-2600) was adopted to test the light absorption properties of the samples. The micro-morphology of the samples and the material interface information were observed using a field emission scanning electron microscopy (FESEM, ZEISS, Sigma SEM300), combined with a high-resolution transmission electron microscopy (HR-TEM, FEI, G2 F30). In the scratch test, the scratched area was analyzed using energy dispersive spectroscopy (EDS) mapping (Hitachi S-3400N).

2.5 Electrochemical testing

The protective capacity of the coating was studied by electrochemical impedance spectroscopy (EIS) and electrochemical testing was performed using a Germany Zahner-Elektrik IM6e electrochemical workstation. The prepared steel plates with different coatings were immersed in 3.5 wt.% NaCl solution at room temperature and tested for EIS at 6, 24, 48, 72 and 168 h, respectively. The test system was a three-electrode system consisting of a working electrode: coated S45C steel plate (effective working area of 2.25 cm^2 immersed in 3.5 wt.% NaCl solution), a reference electrode: saturated calomel electrode (SCE, Hg/Hg_2Cl_2) and an auxiliary electrode: platinum sheet electrode. Set the voltage amplitude to 10 mV and the frequency range from 0.1 Hz to 100 kHz. Each sample was tested 3 times in parallel and the most representative results were selected among them.

2.6 Optical current density versus time (*i–t*), Mott–Schottky (M–S) and cyclic voltammetry (CV) curve test

The optical current density curves and Mott–Schottky curves of the materials were studied by an electrochemical workstation (CHI 760E, Ch Instrument, Shanghai). A three-electrode system was used as the electrochemical workstation system and 0.5 mol·L^{-1} Na_2SO_4 solution was used as the electrolyte solution. We added 10 mg of sample powder to 1 mL of Nafion mixed solution (made by mixing Nafion 117 membrane solution and anhydrous ethanol at a 1:9 ratio by volume) and ultrasonically dispersed. The suspension was then uniformly applied to conductive glass (indium tin oxide (ITO)) as the working electrode, using the SCE (Hg/Hg_2Cl_2) as the reference electrode and platinum sheet electrode as the auxiliary electrode in order to construct the three-electrode system. The scan rate for the *i–t* test was 1 mV·s^{-1}, a 350 W xenon lamp was used as the light source and the light-on interval was set to 20 s. The Mott–Schottky curves were chosen for frequencies of 500, 1000 and 1500 Hz and the voltage range was −1.0 to 1.0 V. The cyclic voltammetry curves were tested using the same three-electrode system with a 3.5 wt.% NaCl electrolyte solution, the scanning rate was chosen to be 50 mV·s^{-1} and the voltage range used was −1.0 to 1.0 V.

3 Results and discussion

3.1 Crystal information, chemical composition and light absorption properties

The major diffraction peaks shown by XRD at 2θ values of 11.32°, 22.47°, 34.68°, 39.81° and 47.56° corresponded to the characteristic (003), (006), (012), (015), and (018) crystallographic facets of the NiAl LDH-like materials [27, 28]. Additionally, two characteristic diffraction peaks near 61° corresponding to (110) and (113) indicated that the LDH nanosheets exhibited typical vertical orientation growth [29], consistent with the standard card spectra of NiAl-LDH (JCPDS#00-015-0087) [30, 31].

As shown in Fig. 1(a), analyzing the characteristic peak intensities of the three LDH samples, NiAl-CO_3^{2-} LDH exhibited the sharpest and most well-formed peaks, indicating excellent crystallinity, while NiAl-MoO_4^{2-} LDH showed relatively weaker and shifted primary diffraction peak intensity. This phenomenon can be attributed to MoO_4^{2-} initially moving into the anionic gallery of LDH during the pH increase of the hydrothermal reaction, leading to differences in synthesis conditions and insertion of anionic species in the interlayer, resulting in a change in the spacing of the main layer [32]. The primary diffraction peaks of the LDH material composited with ZIF-8 corresponded to the diffraction peaks of both ZIF-8 and NiAl-LDH, with the peaks appearing to be shifted as a whole towards higher angle directions.

For FT-IR spectrum of LDH materials NiAl-NO_3^- LDH, NiAl-CO_3^{2-} LDH and NiAl-MoO_4^{2-} LDH, broad peaks with wave numbers located near 1396–1348 cm^{-1} and absorption peaks at 832, 825 and 798 cm^{-1} corresponded to the infrared peaks of the anions (NO_3^-, CO_3^{2-} and MoO_4^{2-}) contained in their interlayer corridors (Fig. 1(b)) [33–35]. Additionally, characteristic peaks at the wave number of 937 cm^{-1} represented the characteristic infrared peaks of MoO_4^{2-} [36, 37]. Absorption peaks near wave numbers of 613, 565 and 433 cm^{-1} resulted from the lattice vibrations of the M–O–M or M–OH bonds (where M is Ni, Al, or Zn) of the LDH [38, 39]. For

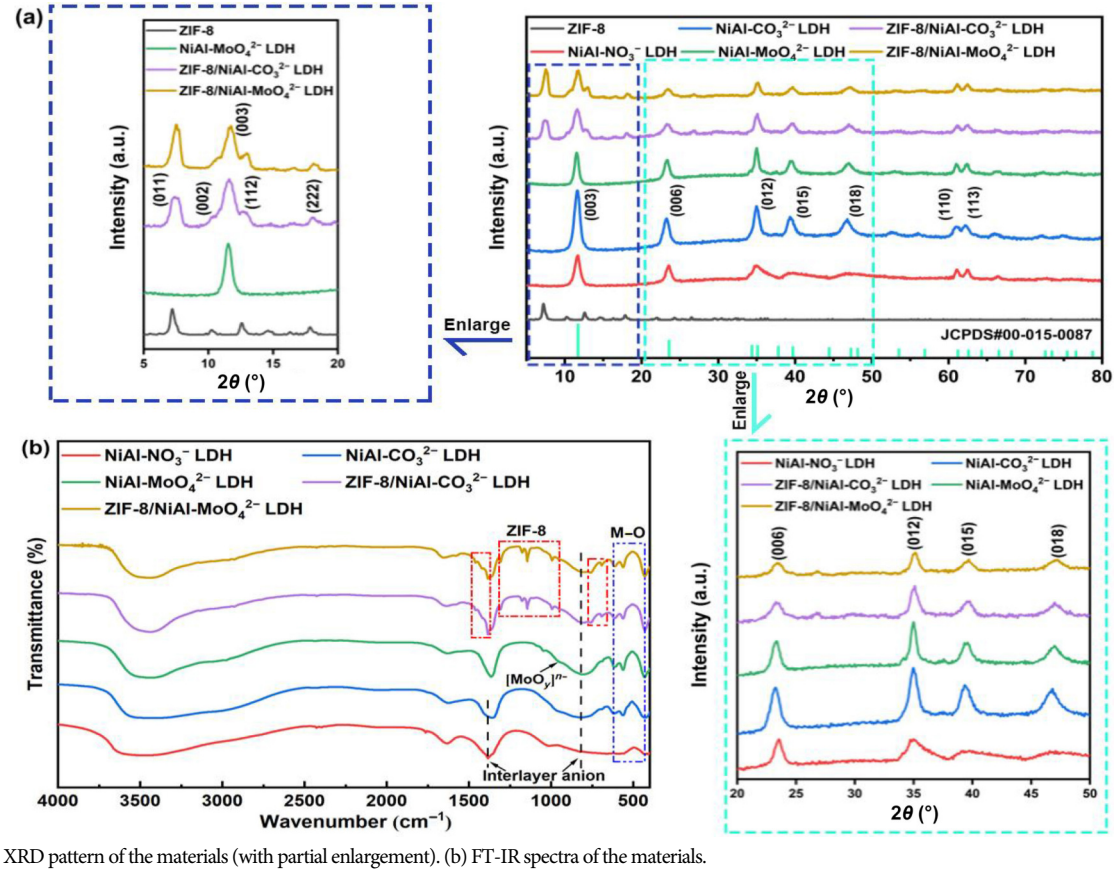

Figure 1 (a) XRD pattern of the materials (with partial enlargement). (b) FT-IR spectra of the materials.

composite ZIF-8/NiAl-CO_3^{2-} LDH and ZIF-8/NiAl-MoO_4^{2-} LDH materials, in addition to the characteristic peaks of LDH, comparison with the non-composite-modified LDH material revealed a strong peak at 1457 cm^{-1} corresponding to the tensile vibration of the imidazole ring. Spectral absorption bands within the wave number range of 1350–900 cm^{-1} were attributed to the in-plane bending vibration of the five-membered nitrogen heterocycle [40]. Furthermore, peaks at 760 and 690 cm^{-1} were related to the bending vibration of the sp^2 hybridized C–H bond [41].

3.2 Elemental analysis of materials

In order to validate the successful synthesis of the material, elemental analysis is imperative. In this work, surface elemental analysis was carried out using XPS, while quantitative elemental content analysis was conducted using ICP-OES.

The elemental composition of the surface materials of the three NiAl LDH and ZIF-8/NiAl LDH composites were characterized by XPS. Analysis of the ZIF-8/NiAl-MoO_4^{2-} LDH material revealed the presence of C, N, O, Al, Ni, Zn and Mo elements on the surface in Fig. 2(a). In the C 1s spectrum (Fig. 2(b)) of ZIF-8/NiAl-CO_3^{2-} LDH and ZIF-8/NiAl-MoO_4^{2-} LDH, the peak near 284.80 eV of binding energy originated from the sp^3 and sp^2 hybridization of the carbon element in the 2-methylimidazole, corresponding to the carbon–carbon bonding of C–C and C=C. Peaks near 285.93 and 288.63 eV corresponded to the carbon–nitrogen bonding of C–N and C=N on the imidazole ring, confirming the successful complexation of ZIF-8 with the LDH material. The peak at 286.25 eV of ZIF-8/NiAl-CO_3^{2-} LDH (attributed to the C=O double bond) was significantly stronger in intensity than that at 286.75 eV of ZIF-8/NiAl-MoO_4^{2-} LDH, indicating the presence of C=O bonding of CO_3^{2-} within the main layer corridors of ZIF-8/NiAl-CO_3^{2-} LDH [42, 43]. Deconvolution peaks of the N 1s spectrum (Fig. S3(a) in the Electronic Supplementary Material (ESM)) of both materials corresponded to the C=N–C in the imidazole ring (398.86 eV) and the N–H bonding of the nitrogen atoms coordinated to the metal center ion Zn^{2+} (399.73 eV) [44]. In the O 1s spectrum (Fig. 2(c)), a single peak at 531.69 eV indicated the hydroxyl peak on the main laminate of the layered double hydroxide cation, corresponding to the M–O–H bond (M is the metal cation) (Fig. S3(b) in the ESM) [39]. The Zn 2p spectrum revealed peaks at 1021.59 and 1044.63 eV for the Zn $2p_{3/2}$ and $2p_{1/2}$ peaks of ZIF-8/NiAl-CO_3^{2-} LDH, respectively. For ZIF-8/NiAl-MoO_4^{2-} LDH, peaks were observed at 1021.81 and 1044.81 eV for the Zn $2p_{3/2}$ and $2p_{1/2}$ peaks, respectively [45]. This shift of about 0.2 eV in binding energy may be attributed to the presence of MoO_4^{2-} in the interlayer. Specifically, after compounding with ZIF-8, the peak width of the Mo 3d XPS spectrum narrowed, indicating that the ZIF-8 compound enhances the uniformity of the electronic state of Mo within the NiAl LDH structure (Fig. 2(d)). The Al 2p and Ni 2p spectra of ZIF-8/NiAl-MoO_4^{2-} LDH exhibited characteristic peaks (Figs. S4(c) and S4(d) in the ESM) [46, 47]. These results from XPS analysis further confirmed the successful synthesis of the material.

After performing surface elemental analysis of the material using XPS, to further corroborate the successful synthesis of the material, ICP-OES testing was conducted on the target product, ZIF-8/NiAl-MoO_4^{2-} LDH. This testing provided quantitative analysis of elements such as Zn, Al, Ni and Mo elements present in the material (Table 1). Notably, the mass fraction ratio of Ni element to Al element was found to be 6.61, which aligns with the standard

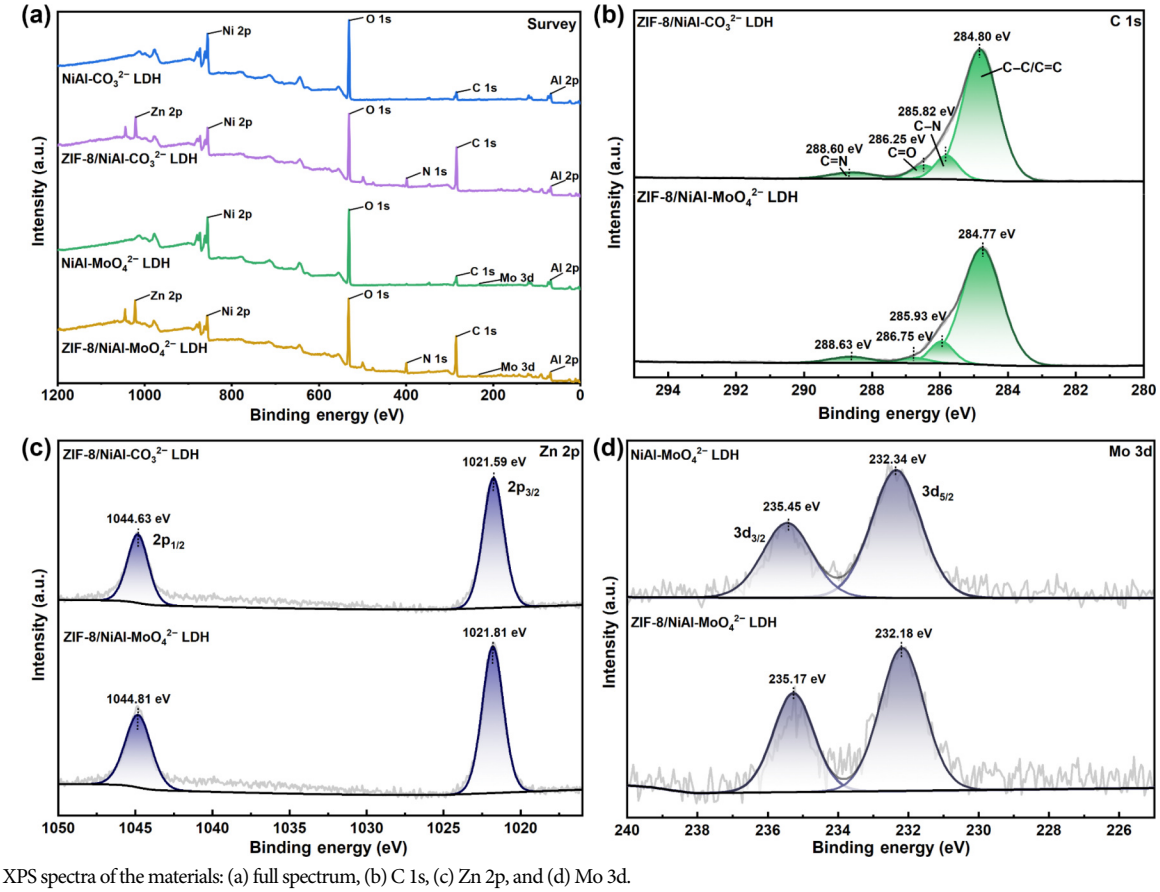

Figure 2 XPS spectra of the materials: (a) full spectrum, (b) C 1s, (c) Zn 2p, and (d) Mo 3d.

Table 1 The elemental content of ZIF-8/NiAl-MoO_4^{2-} LDH as determined by ICP-OES

Elemental	Sample elemental content ($mg \cdot g^{-1}$)	Percentage of quality (%)
Zn	78.51	7.85
Al	48.60	4.86
Ni	321.24	32.12
Mo	8.18	0.82

card of NiAl-LDH (JCPDS#00-015-0087), further confirming the successful synthesis of LDH. Additionally, the presence of the Mo element partially indicates the successful intercalation of MoO_4^{2-} between the layers.

3.3 Characterization of material microstructure morphology

In order to gain a deeper understanding of the synthesis of the material and provide a basis for its corrosion resistance mechanism, the characterization of the material's microstructure morphology is essential.

As seen from the SEM images, the average particle size of the ZIF-8 nanoparticles used for comparison was approximately 600–800 nm, displaying the characteristic stereo configuration of a dodecahedral zeolitic imidazolate frameworks material (Fig. S4(a) in the ESM) [48]. The NiAl-NO_3^- LDH material, synthesized with NaOH as a precipitant, exhibited a block structure with irregular morphology, variable sizes and varying thicknesses of laminated stacks (Fig. S4(d) in the ESM). In contrast, NiAl-CO_3^{2-} LDH and NiAl-MoO_4^{2-} LDH, synthesized using urea as the precipitant, demonstrated uniform nanosheet stacked structures with sheet sizes of approximately 200–400 nm and thicknesses of about 20–30 nm (Figs. S4(e) and S4(f) in the ESM) [49]. This homogeneous morphology was attributed to the synthesis process, where NH_4F initially formed complex ions with Ni^{2+} and Al^{3+}, followed by the gradual decomposition of urea into NH_3, creating a buffer solution with NH_4^+ and NH_3 to facilitate the gradual dissociation and precipitation of Ni^{2+} and Al^{3+}, resulting in thin nanosheets [50]. The tighter, thinner nanosheet stacked morphology exhibited fewer voids compared to the block stacked morphology. However, NiAl-CO_3^{2-} LDH and NiAl-MoO_4^{2-} LDH still retained a part of the flower-like cluster structure with easily penetrable voids at bonding sites, allowing corrosive substances such as OH^- and Cl^- to attack the substrate surface when exposed to corrosive media.

As shown in Figs. S4(b) and S4(c_1) in the ESM, the ZIF-8 nanoparticles, with an average particle size of about 50–70 nm, were uniformly compounded on the surface of NiAl LDH nanosheets with a thickness of about 20 nm, forming a ZIF-8/NiAl LDH composite with ample nanocontainers and more detailed morphology of the nanocontainer can be observed from Fig. S4(c_2) in the ESM. Unlike the typical dodecahedral zeolite imidazolate framework material of ZIF-8, the composite ZIF-8/NiAl LDH material exhibited a relatively flat morphology. The ZIF-8 is homogeneously loaded on the LDH and the surface structure effectively fills the voids in the original NiAl LDH flower cluster structure, resulting in a denser composite structure and reducing the possibility of corrosive media penetration.

The morphology observed in TEM images (Figs. 3(a) and 3(b)) was consistent with SEM images (Figs. S4(b) and S4(c) in the ESM), showing tightly bonded lamellar NiAl LDH nanomaterials with granular ZIF-8. By combining HR-TEM images with GMS 3 software, the crystallographic spacing d(012) of the NiAl LDH

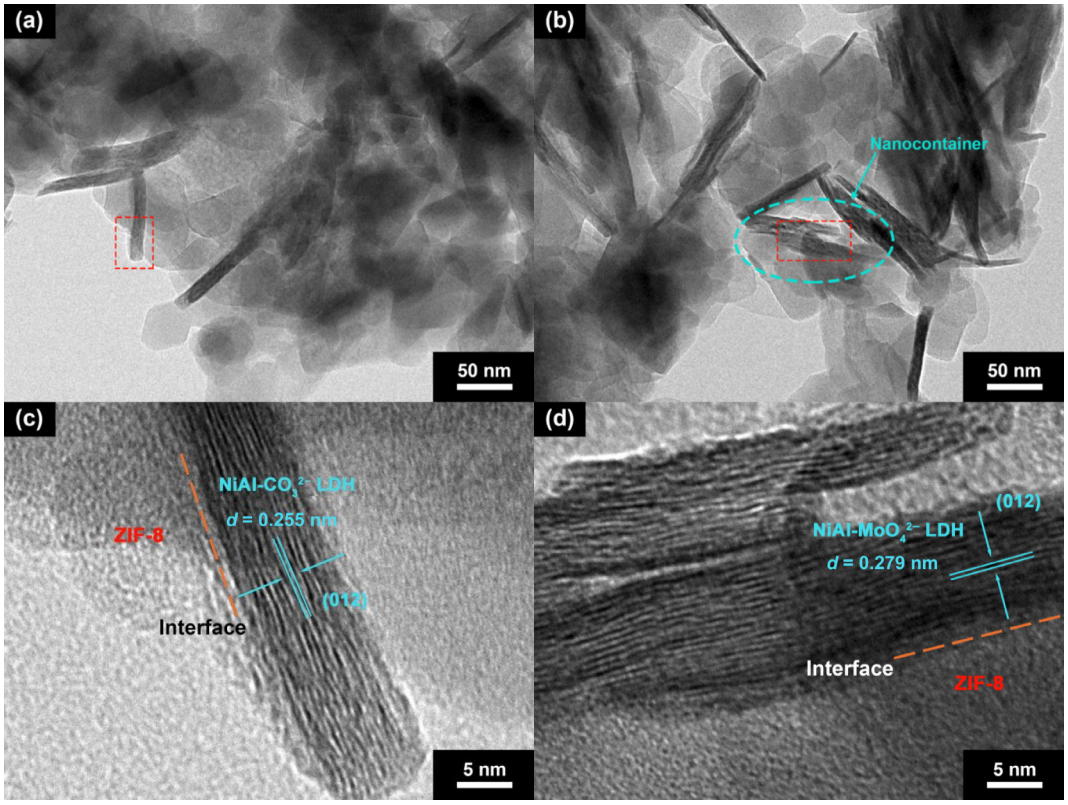

Figure 3 TEM images of materials: (a) ZIF-8/NiAl-CO_3^{2-} LDH and (b) ZIF-8/NiAl-MoO_4^{2-} LDH. HR-TEM images: (c) ZIF-8/NiAl-CO_3^{2-} LDH and (d) ZIF-8/NiAl-MoO_4^{2-} LDH.

material (012) was determined. The crystallographic spacing of ZIF-8/NiAl-CO_3^{2-} LDH material was measured at 0.255 nm, while that of ZIF-8/NiAl-MoO_4^{2-} LDH material was found to be 0.279 nm, aligning closely with literature values (Figs. 3(c) and 3(d)) [33]. The variance in crystal plane spacing could be attributed to differences in urea dosage and the radius of the intercalated anion, with MoO_4^{2-} having a larger radius than CO_3^{2-}. The numerical increase in the d(012) spacing of NiAl LDH enhanced the ability of the nanocontainers to capture Cl^- when incorporating LDH with larger radius interlayer anions, simultaneously indicating the successful integration of MoO_4^{2-} into the main interlayer corridor of NiAl LDH [51].

3.4 Enhancement of thermal property

The synthesis of ZIF-8/NiAl-MoO_4^{2-} LDH also enhances the thermal stability. TG-differential TG (TG-DTG) curves of NiAl-CO_3^{2-} LDH and NiAl-MoO_4^{2-} LDH exhibited similar trends in Figs. 4(a) and 4(b), displaying three-stage mass loss curves at 26.9–224.6, 224.5–300.2 and 300.2–597.4 °C, with mass losses of approximately 11.78%, 4.42% and 16.72%, respectively. These stages corresponded to the loss of water of crystallization, the removal of interlayer anions and the decomposition of the cationic main layer into layered oxides, representing three thermal decomposition processes in the NiAl LDH material, with a total mass change rate of about 34% [52]. Similarly, TG-DTG weight loss curves of the ZIF-8/NiAl LDH material were segmented into three stages (Figs. 4(c) and 4(d)). The initial stage involved the loss of water of crystallization (30.3–241.6 °C, 7.22% mass loss), followed by the removal of anions from the main layer gallery (241.6–390.5 °C, 23.65% mass loss) and finally, the decomposition of hydroxyl groups in the main layer of the cationic cation along with the thermal decomposition of surface-deposited ZIF-8 (390.5–597.2 °C, 11.97% mass loss).

The analysis of the differential scanning calorimetric (DSC) curves (Fig. 4(e)) provided insight into the heat flow changes during

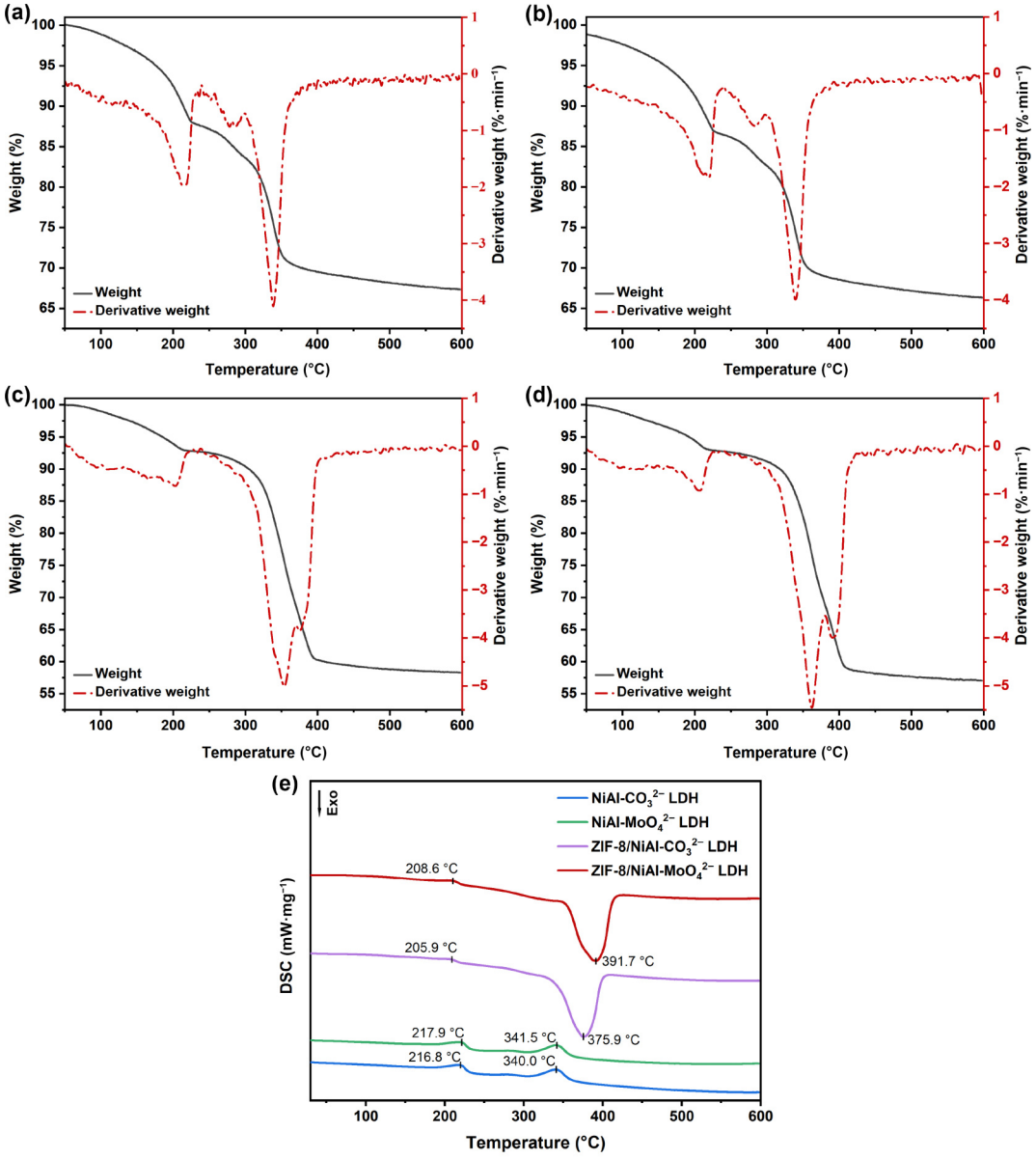

Figure 4 TG-DTG curves of materials: (a) NiAl-CO_3^{2-} LDH, (b) NiAl-MoO_4^{2-} LDH, (c) ZIF-8/NiAl-CO_3^{2-} LDH, and (d) ZIF-8/NiAl-MoO_4^{2-} LDH. (e) DSC curves of the materials.

thermal decomposition. The initial mass loss observed on the DSC curves of the composites occurred earlier than that of the single LDH material, possibly due to the surface adsorption of trace moisture by ZIF-8, leading to early-stage mass loss with temperature increase. NiAl-MoO_4^{2-} LDH exhibited a higher thermal decomposition temperature compared to NiAl-CO_3^{2-} LDH, with both showing upward peaks in their DSC curves, indicative of a heat absorption process. Conversely, the third weight-loss stage of ZIF-8/NiAl-CO_3^{2-} LDH and ZIF-8/NiAl-MoO_4^{2-} LDH exhibited an exothermic process, suggesting the production of organic ligands during Zn-metal-organic framework (MOF) decomposition, which carbonized and combusted at high temperatures [53]. The third weight loss decomposition temperature of ZIF-8/NiAl-MoO_4^{2-} LDH was higher than that of ZIF-8/NiAl-CO_3^{2-} LDH, indicating tighter bonding of ZIF-8 to NiAl-MoO_4^{2-} LDH and relatively better thermal stability.

3.5 Research on corrosion protection performance

As a corrosion-resistant coating, its most critical evaluation criterion is corrosion resistance. In this work, Nyquist impedance plots and bode/phase angle plots were obtained through EIS testing for iron blocks coated with epoxy coatings and immersed in 3.5 wt.% NaCl solution over different time periods. These electrochemical data were then fitted using electrochromic materials (ECMs) to calculate the total impedance values, allowing for a quantitative assessment of the protective capability.

The semicircular arcs shown in Nyquist plots (Fig. S5 in the ESM and Fig. 5) indicated that an electrochemical corrosion process occurred at the metal/electrolyte interfaces and that this process was primarily controlled by charge transfer impedance. Frequency errors occurred in all of the three-electrode systems used due to the uneven surface roughness of the electrodes and thus the Nyquist curves showed irregular or incomplete semicircular or circular arcs [54]. The real and imaginary impedance values of the composite coating with the addition of LDH were significantly higher than those of the pure epoxy coating for the immersion period and the impedance performance of ZIF-8/NiAl-MoO_4^{2-} LDH was more potent than that of all other materials. It proved that the designed ZIF-8 surface self-assembly composite effectively enhanced the interfacial compatibility of LDH nanocontainers inside the coating, which can constitute the densest structure to effectively fill the coating defects and the bimetallic cationic main layer structure can also effectively impede the charge transfer process between the metal/electrolyte interfaces to achieve the optimal corrosion protection effect.

The frequencies corresponding to the maximum phase angles of all coatings in the plots gradually decreased as the corrosive ions continued to attack, indicating a decrease in the degree of coating integrity (Fig. S6 in the ESM and Fig. 5(b)). The phase angle of ZIF-8/NiAl-MoO_4^{2-} LDH at 72 h exhibited the highest value in the medium-high frequency region ($f = 10^3$–10^4 Hz) and had the largest impedance modulus in the low-frequency region of all coatings at all times, indicating the most effective resistance to the charge and ion transfer process at the metal/electrolyte interface [55].

Equivalent circuit models were used to fit the EIS results and due to the anodic inhibition of passivation effect within the MoO_4^{2-} LDH nanocontainers, both NiAl-MoO_4^{2-} LDH and ZIF-8/NiAl-MoO_4^{2-} LDH coatings were fitted and calculated by Model 2, while the rest of the coatings were fitted by Model 1 (Fig. 5(c)). All the

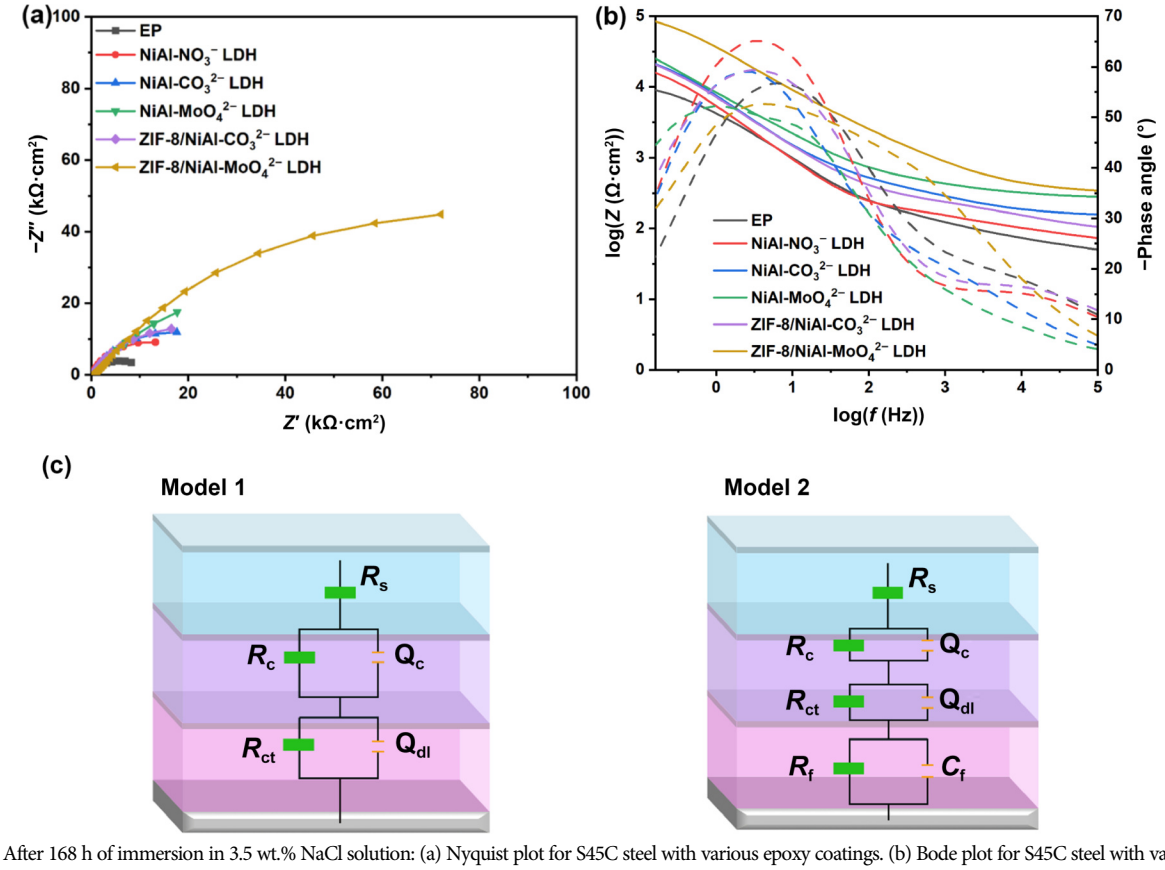

Figure 5 After 168 h of immersion in 3.5 wt.% NaCl solution: (a) Nyquist plot for S45C steel with various epoxy coatings. (b) Bode plot for S45C steel with various epoxy coatings. (c) Equivalent circuit model.

fitted parameters with the total impedance values were calculated (Eqs. (11) to (14)) [56]. After 168 h of immersion, the impedance properties of NiAl-MoO_4^{2-} LDH composite epoxy coatings had been enhanced to 409.8%, 201.0% and 150.4% compared to EP, NiAl-NO_3^- LDH and NiAl-CO_3^{2-} LDH, indicating the effectiveness of the corrosion inhibitor nanocontainers (Table 2). The total impedance value of ZIF-8/NiAl-MoO_4^{2-} LDH composite epoxy coating was higher by an order of magnitude compared to ZIF-8/NiAl-CO_3^{2-} LDH composite epoxy coating and reached 593.8% of the total impedance value of NiAl-MoO_4^{2-} LDH coating. The total impedance value of ZIF-8/NiAl-MoO_4^{2-} LDH was increased to 2843.1% of its value relative to that of ordinary EP coatings, which indicated the designed ZIF-8/NiAl-MoO_4^{2-} LDH heterojunction vessel was able to significantly attenuate the corrosion of S45C steel in high salt environments with excellent long-lasting protection

$$Z_Q = Y\omega^n \tag{11}$$

$$Z_1 = R_s + \frac{1}{\frac{1}{R_c} + \frac{1}{Z_{Qc}}} + \frac{1}{\frac{1}{R_{ct}} + \frac{1}{Z_{Qdl}}} \tag{12}$$

$$Z_2 = R_s + \frac{1}{\frac{1}{R_c} + \frac{1}{Z_{Qc}}} + \frac{1}{\frac{1}{R_{ct}} + \frac{1}{Z_{Qdl}}} + \frac{1}{\frac{1}{R_f} + \frac{1}{C_f}} \tag{13}$$

$$\omega = 2\pi f \tag{14}$$

The meaning each symbol stands for: conductance (Y), the calculated Y values for Z_{Qc} and Z_{Qdl} are Y_1 and Y_2, angular frequency (ω), dispersion index (n), the calculated n values for Z_{Qc} and Z_{Qdl} are n_1 and n_2, solution resistance (R_s), coating resistance (R_c), constant phase angle element of coating (Qc), charge transfer resistance (R_{ct}), constant phase angle element of electrical double layer (Qdl), passivation film resistance (R_f), passivation film element capacitance (C_f) and total impedance (Z). In the formula, Z_Q is the capacitive impedance, Z_1 is the total impedance of Model 1 and Z_2 is the total impedance of Model 2. In In the ECM model, the parentheses () indicate a parallel connection, R represents the resistance element, C represents the capacitance element and Q represents the constant phase angle element in the ECM model.

3.6 Scratch experiments

In evaluating the durability and protective efficacy of coatings in practical applications, where physical abrasions and scratches are inevitable, it is imperative to assess their performance under such conditions. To this end, a scratch test was conducted specifically to examine the protective capabilities of a ZIF-8/NiAl-MoO_4^{2-} LDH coating applied to metal substrates.

The test involved artificially inducing scratches on the coating surface and subsequently immersing the scratched samples in a 3.5 wt.% NaCl solution for 168 h, simulating a corrosive environment. Following the immersion period, SEM and EDS mapping were employed to analyze the scratched area (Fig. 6).

The SEM and EDS spectra indicate that the distribution of C and O elements aligns well with the epoxy resin present in the coating. Furthermore, the presence and distribution of nickel and aluminum elements from LDH within the coating coincide with that of the epoxy resin, suggesting a relatively uniform dispersion of LDH throughout the coating matrix.

Notably, Mo element displayed a more extensive distribution within the scratched region compared to Ni and Al elements. This observation suggests that the MoO_4^{2-} ions, initially intercalated between LDH layers, have been released and reacted to form a stable compound on the surface of the scratch. The similarity in distribution patterns between Mo and Fe elements within the scratched area further implies the formation of an iron molybdate passivation film. Such a film acts as an effective barrier, providing enhanced protection against corrosion within the scratched area.

Therefore, the results conclusively demonstrate that the ZIF-8/NiAl-MoO_4^{2-} LDH coating retains its superior protective performance for the underlying metal substrate, even after experiencing physical damage in the form of scratches. This finding underscores the potential of ZIF-8/NiAl-MoO_4^{2-} LDH for enhancing the durability and longevity of metal components in various industrial and environmental applications.

3.7 Investigation of the anti-corrosion mechanism of heterojunction nanocontainers

The synergistic corrosion protection mechanism of ZIF-8/NiAl-MoO_4^{2-} LDH was schematically shown in Fig. 7, mainly composed of the following three aspects of protection.

Table 2 The calculated data of fitted electrochemical parameters of S45C coated with different epoxy coatings after immersion in 3.5 wt.% NaCl solution for 168 h

Sample	EP	NiAl-NO_3^- LDH	NiAl-CO_3^{2-} LDH	ZIF-8/NiAl-CO_3^{2-} LDH	NiAl-MoO_4^{2-} LDH	ZIF-8/NiAl-MoO_4^{2-} LDH
ECM			R(QR)(QR)			R(QR)(QR)(CR)
R_s ($\Omega\cdot cm^2$)	37.81	54.48	141.00	75.99	250.90	302.00
Y_1 ($\Omega^{-1}\cdot cm^{-2}\cdot s^{-n}$)	4.76×10^{-5}	3.74×10^{-5}	2.89×10^{-5}	3.25×10^{-5}	3.36×10^{-5}	1.09×10^{-5}
n_1	0.76	0.83	0.80	0.75	0.71	0.84
R_c ($\Omega\cdot cm^2$)	1.15×10^4	2.40×10^4	3.27×10^4	3.90×10^4	7.62×10^4	4.65×10^4
Y_2 ($\Omega^{-1}\cdot cm^{-2}\cdot s^{-n}$)	1.20×10^{-4}	6.60×10^{-5}	7.68×10^{-5}	3.67×10^{-6}	1.22×10^{-4}	1.82×10^{-5}
n_2	0.47	0.48	0.49	0.49	0.41	0.52
R_{ct} ($\Omega\cdot cm^2$)	1.19×10^2	1.35×10^2	4.22×10^2	1.95×10^2	3.88×10^2	2.47×10^5
C_f ($F\cdot cm^{-2}$)	—	—	—	—	4.51×10^{-5}	8.93×10^{-6}
R_f ($\Omega\cdot cm^2$)	—	—	—	—	4.63×10^2	7.24×10^1
Chi-squared	3.76×10^{-4}	3.41×10^{-4}	6.15×10^{-5}	2.60×10^{-5}	4.71×10^{-5}	3.87×10^{-5}
Z ($\Omega\cdot cm^2$)	1.02×10^4	2.08×10^4	2.78×10^4	2.94×10^4	4.18×10^4	2.90×10^5

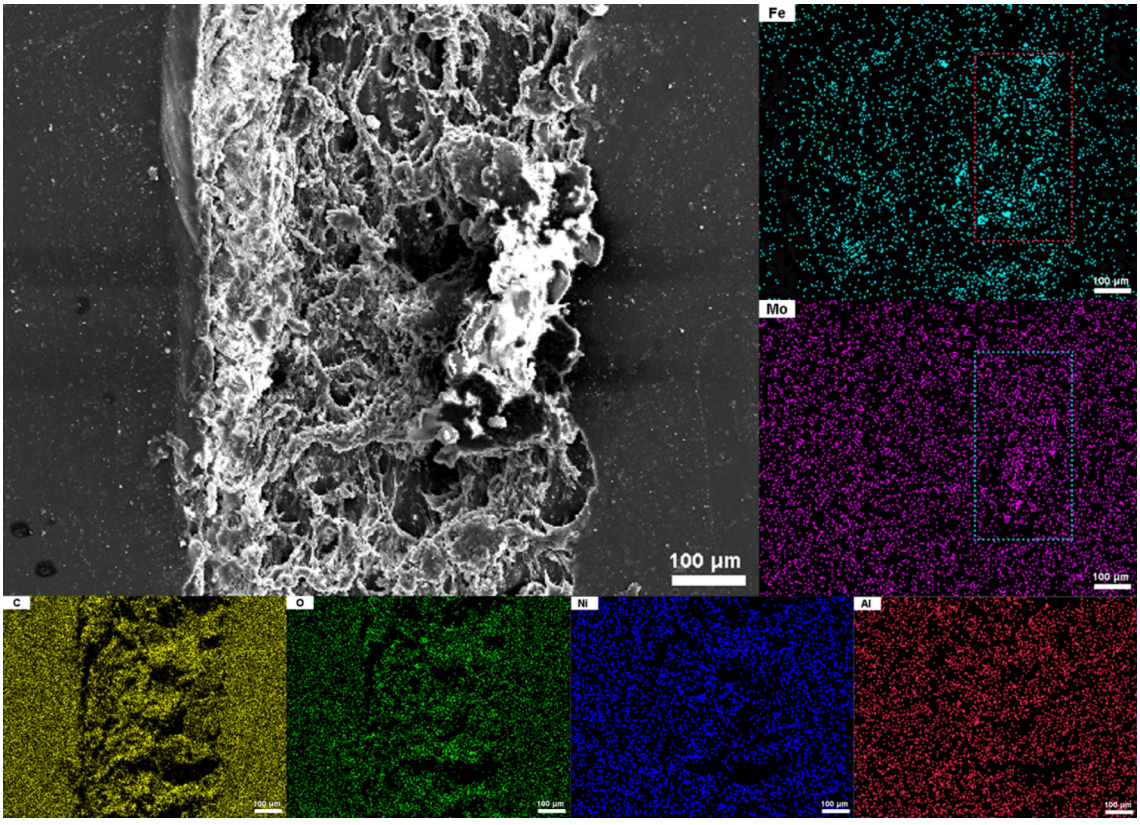

Figure 6 SEM images and EDS mapping images of scratches on the ZIF-8/NiAl-MoO_4^{2-} LDH coating after immersion in 3.5 wt.% NaCl solution for 168 h.

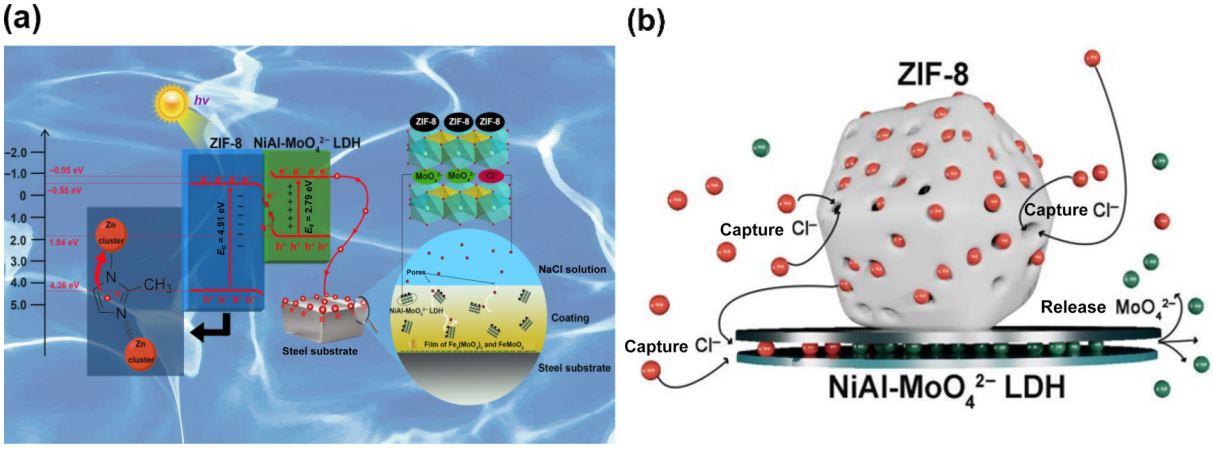

Figure 7 (a) Schematic of synergistic anti-corrosion mechanism for ZIF-8/NiAl-MoO_4^{2-} LDH. (b) Schematic diagram of the nanocontainer structure.

3.7.1 Controlled corrosion inhibitor release and corrosion ion capture protection

The LDH material has an unique ion exchange capability due to its unique cationic lamellar corridor structure, which gives it a unique role as a corrosion-resistant nano-unit for ion traps and corrosion inhibitor containers [57, 58]. It can continuously capture Cl^- ions in the intruding medium, blocking the diffusion path of Cl^- and preventing its adsorption on the metal surface and corrosion reaction. The interlayer-released MO_4^{2-} adsorbed and formed a protective composite passivation film on the surface of the S45C carbon steel where pitting occurred, providing sufficient initial protection for the pitting site.

Despite the synergistic protective effects such as compatibility improvement and densification enhancement, the impedance values of ZIF-8/NiAl-CO_3^{2-} LDH at 72–168 h were only equal to NiAl-CO_3^{2-} LDH and weaker than those of NiAl-MoO_4^{2-} LDH coatings, which proved the effective inhibition of MoO_4^{2-} for metal corrosion and demonstrated better synergy between MO_4^{2-} and ZIF-8 (Fig. 8). Unlike NiAl-CO_3^{2-} LDH and NiAl-MoO_4^{2-} LDH, ZIF-8/NiAl-MoO_4^{2-} LDH composite coating had an extremely high impedance at the beginning of the immersion and the NiAl-MoO_4^{2-} LDH also showed excellent protective properties at 24 h (Fig. S5(b) in the ESM). This suggested that the formation of insoluble iron molybdate passivation film by MoO_4^{2-} (through Eqs. (15) and (16)) can produce an effective anodic inhibition effect on S45C, reduce the buildup of corrosion products such as Fe_3O_4, γ-FeOOH, at the metal/electrolyte interface and prevented photocorrosion of iron

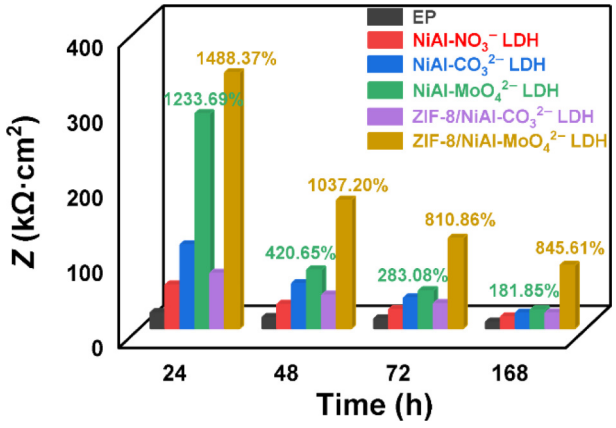

Figure 8 Columnar comparison of impedance values for each coating at different time intervals.

oxides in the light, which prolonged the corrosion prevention time limit of the coating [59]. However, during 24–168 h, the NiAl-MoO_4^{2-} LDH coating showed a rapid decrease in impedance value, which eventually became equivalent to the other coatings at 168 h (Fig. 5(a) and Figs. S5(b)–S5(d) in the ESM). This may be because with the increase in immersion time, the main layer structure of the LDH material was damaged, which resulted in the corrosive substances in the ionic traps being re-released to the metal surface, causing the subsequent corrosion of the metal substrate. However, the impedance value of ZIF-8/NiAl-MoO_4^{2-} LDH coating maintained a steadier trend, exhibiting stable and excellent protection characteristics

$$2Fe^{3+} + 3MoO_4^{2-} \rightarrow Fe_2(MoO_4)_3 \quad (15)$$

$$Fe^{2+} + MoO_4^{2-} \rightarrow FeMoO_4 \quad (16)$$

The adsorption properties and specific surface area were investigated by BET tests, the protective properties of the ZIF-8/NiAl-MoO_4^{2-} LDH coatings were further explored. As shown in Fig. S7 in the ESM, the specific surface area, pore volume and microporous volume of the NiAl LDH material gradually increased with the rise of anion volume, which was consistent with the HR-TEM characterization results, indicating that the increase of interlayer spacing can enhance the specific surface area. The adsorption isotherms of the composites were all of type IV and have H4 hysteresis loops [38]. The materials exhibited a significant increase in microporous pore volume, indicating that the composite of ZIF-8 provided adequate surface micropores. Therefore, the high specific surface area NiAl-MoO_4^{2-} LDH nanosheets synergized with ZIF-8, which contained a large number of unique microporous structures, can constitute a composite nanocontainer with active protection capability. As a supramolecular valve for the corrosion inhibitor MoO_4^{2-}, the adsorption of OH^- and Cl^- can be accelerated upon contact with corrosive media, reinforcing the stimulant-responsive release mechanism of MoO_4^{2-} with the ion-trapping function of the nanocontainer, increase in the early stage of corrosion MoO_4^{2-} release ability and the ability to capture the removal of corrosive ions, enhance the passivation protection for the beginning of pitting corrosion, from the early stage of corrosion in time to reduce the possibility of subsequent corrosion, ZIF-8/NiAl-MoO_4^{2-} LDH corrosion inhibitor active response to the release of the protection of the ion capture so that it has the best anticorrosive properties. In addition, the surface self-assembly ZIF-8 is tightly bound to the LDH, providing protection for the LDH main layer and reducing the structural breakdown of the main layer due to prolonged immersion.

3.7.2 *Photoelectric corrosion protection effect*

Photogenerated currents originating from the excitation of the semiconductor material itself in the presence of light provide additional protection to the metal substrate without additional energy consumption. As photocurrent density curves showed, owing to the increase of specific surface area after ZIF-8 composited, the active surface sites and the number of highly active atoms of the heterojunction materials increased, the photoelectric activity of the heterojunction materials was enhanced (Fig. 9(a)). ZIF-8/NiAl-MoO_4^{2-} LDH possessed the maximum photogenerated current density value, which can reach about 700 nA·cm^{-2} in 220 s and the excited photocurrents in the rest of the time were all higher than 300 nA·cm^{-2}. In contrast, the photogenerated current densities of the non-composite LDH material and the ZIF-8 material were always lower than 200 nA·cm^{-2}, which suggested that the construction of the heterojunction structure of the MOFs with the NiAl LDH material can effectively enhance the effect of the photocathode protection.

Characterizing the energy band structure of the heterojunction by Mott–Schottky test and XPS valence band (VB) spectra, for n-type semiconductors, the flat band potential (E_{fb}) of the M–S curve can be considered as the value of the conduction band potential (E_{CB}). The corresponding E_{fb} values of the materials can be obtained by making the intersection of the epitaxial lines of the straight line segments at the inflection points of the M–S curves at three different frequencies with the X-axis [60] (Figs. 9(b)–9(e)). A tangent to the XPS valence band spread curve of the solid material can then be calculated to obtain the valence band top potential (E_{VB}) of the solid material [61] (Fig. 9(f)). The material forbidden bandwidth E_g can be obtained (Eq. (17))

$$E_g = E_{VB} - E_{CB} \quad (17)$$

Combined with the above characterization results, the heterojunction energy band structure as well as the schematic diagram of the charge transfer mechanism during the photoprotection process were obtained (Fig. 7(a)). The monomer functional group of the organic ligand 2-methylimidazole undergoes a charge transfer process specific to MOFs upon photoexcitation that causes photogenerated electrons to delocalize from the π-bonding orbitals on the ring of 2-methylimidazole and underwent the process of electron leaps toward the 3p orbitals of the nearest metal body, Zn^{2+}. Subsequently, they were transferred to the composite interface to complex with h^+ generated in the conduction band of the LDH material. In contrast, the photogenerated electrons generated on the LDH are transferred to the surface of the iron substrate with a much lower potential, constituting a complete Z-type heterojunction structure and forming a photogenerated cathodic protection effect. In addition, the organic ligand 2-methylimidazole has excellent UV light utilization ability, which enhances the coating's resistance to UV light and enhances the coating's weatherability.

3.7.3 *ZIF-8 hydrophobicity and N–H co-curing effects*

LDH materials are inorganic materials with superhydrophilicity due to a huge number of hydroxyl groups in the cationic main laminate, so they are easy to be aqueous media. For organic coatings, the

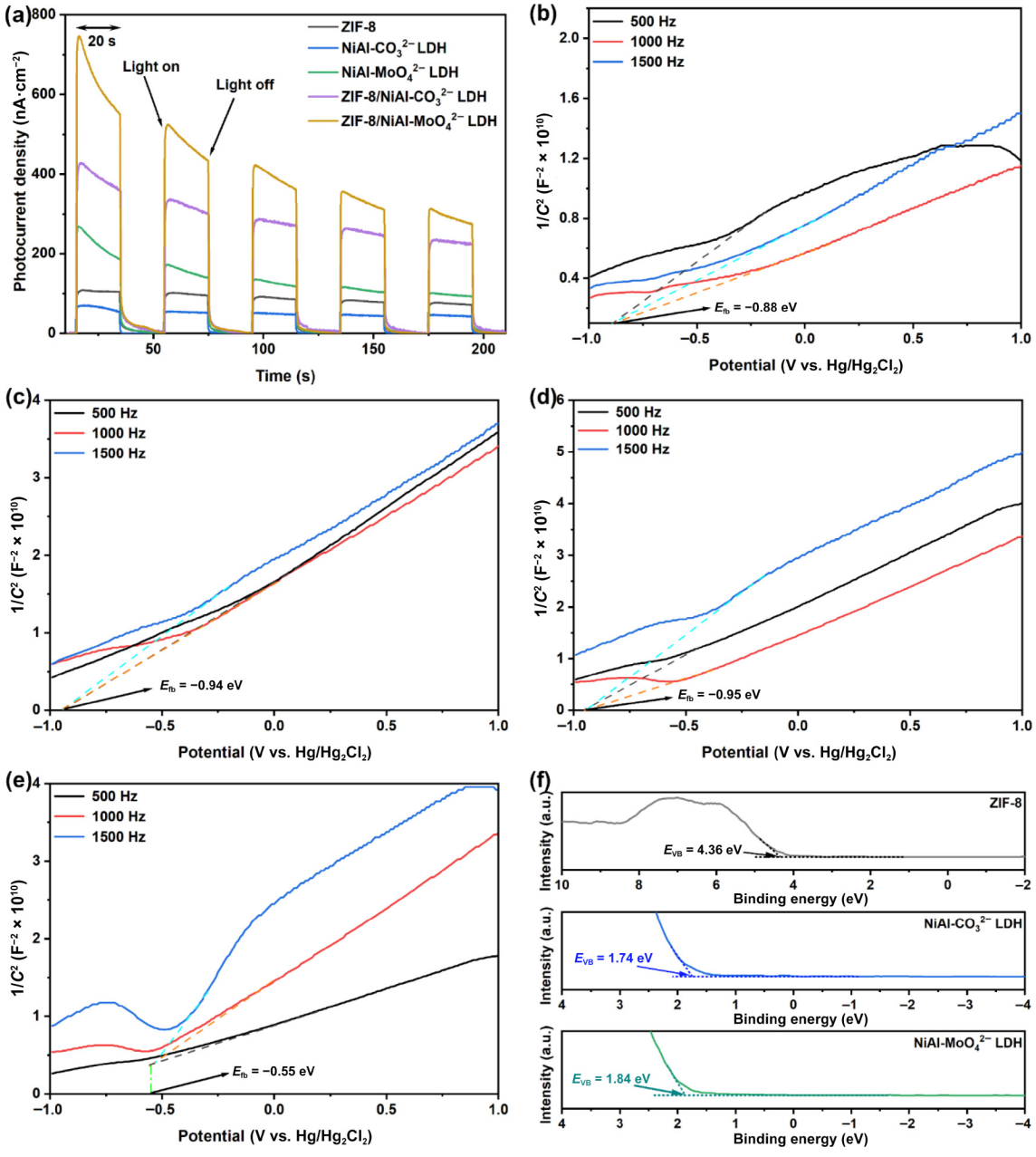

Figure 9 (a) Photocurrent density curves. M–S curves of different materials: (b) NiAl-NO_3^- LDH, (c) NiAl-CO_3^{2-} LDH, (d) NiAl-MoO_4^{2-} LDH, and (e) ZIF-8. (f) XPS valence band spectra.

introduction of superhydrophilic materials will accelerate the penetration of corrosive media, so weakening the hydrophilicity can enhance the overall protective effect of the coating. ZIF-8 has the porous structure and high specific surface area of zeolite-like materials, which can enhance the roughness of the composite surface. The ligand bonding angle between the metal body Zn^{2+} and the N atom on the 2-methylimidazole of the organic ligand is similar to that of the 145° Si–O–Si bonding angle of the zeolite-like material, so it has a excellent hydrophobicity and the superhydrophilic property of LDH can be effectively cut down after composite with LDH. Both ZIF-8/NiAl-CO_3^{2-} LDH and ZIF-8/NiAl-MoO_4^{2-} LDH exhibit smaller surface energies compared to other materials without ZIF-8 composites, indicating that the ZIF-8 composites improve the hydrophobicity of the materials, which is consistent with the water contact angle (WCA) values (Fig. S9 in the ESM). In addition, the interfacial compatibility of the materials also affected the integrity of the coating and the organic ligand 2-methylimidazole was super lipophilic, which enhanced the interfacial compatibility of the inorganic LDH materials with the organic coatings. The N–H bond on the surface of ZIF-8, which was not involved in coordination, can also be involved in the ring-opening polymerization curing process of epoxy resin epoxy bond as a co-curing agent, which enhanced the degree of cross-linking of the epoxy resin, improved the degree of densification of the cured coating and stabilized the ability of the LDH two-dimensional nanosheets to fill defects in the coating, which synergistically improved the overall protective performance of the composite coating.

4 Conclusion

Z-type heterojunction anti-corrosion nanocontainers were

successfully constructed by loading the corrosion inhibitor MoO_4^{2-} ions into nickel-based NiAl LDH material and integrating the metal-organic framework material ZIF-8 through a surface self-assembly approach. As the experimental result showed that the total impedance of the ZIF-8/NiAl-MoO_4^{2-} LDH coating reached 28.43 times of that of the EP after 168 h, which realized a desirable corrosion protection effect. This design strategy, combining dense corrosion inhibitor nanocontainers with self-supported heterojunction structures, provides valuable insights for the development of novel molybdate active corrosion inhibitor nanocontainers and exploration of extending combined active corrosion protection functions.

Electronic Supplementary Material: Supplementary material (Figs. S1–S9) is available in the online version of this article at https://doi.org/10.26599/NR.2025.94907000.

Data availability

All data needed to support the conclusions in the paper are presented in the manuscript and/or the Electronic Supplementary Material. Additional data related to this paper may be requested from the corresponding author upon request.

Acknowledgements

This work was supported by the National Natural Science Foundation of China (No. 22378124) and the Opening Project of Material Corrosion and Protection Key Laboratory of Sichuan Province (No. 2023CL04).

Declaration of competing interest

All the contributing authors report no conflict of interests in this work.

Author contribution statement

Y. M.: Conceptualization, formal analysis, validation, data curation, writing – original draft, writing – review & editing. T. L.: Investigation, data curation, writing – review & editing. S.-R. Z.: Data curation, writing – review & editing. Z.-T. F.: Writing – review & editing. J.-K. L.: Resources, supervision, project administration, writing – review & editing. All the authors have approved the final manuscript.

Use of AI statement

None.

References

[1] Abrantes Leal, D.; Sousa, I.; Bastos, A. C.; Tedim, J.; Wypych, F.; Bruno Marino, C. E. Combination of layered-based materials as an innovative strategy for improving active corrosion protection of carbon steel. *Surf. Coat. Technol.* **2023**, *473*, 129972.

[2] Prabhu, S.; Maruthapandi, M.; Durairaj, A.; Luong, J. H. T.; Gedanken, A. Enhanced electrochemical performance of CuO Capsules@CDs composites for solid-state hybrid supercapacitor. *Energy Fuels* **2023**, *37*, 6824–6833.

[3] Mohammadi, I.; Izadi, M.; Shahrabi, T.; Fathi, D.; Fateh, A. Enhanced epoxy coating based on cerium loaded Na-montmorillonite as active anti-corrosive nanoreservoirs for corrosion protection of mild steel: Synthesis, characterization, and electrochemical behavior. *Prog. Org. Coat.* **2019**, *131*, 119–130.

[4] Kim, M.; Brewer, L. N.; Kubacki, G. W. Microstructure and corrosion resistance of chromate conversion coating on cold sprayed aluminum alloy 2024. *Surf. Coat. Technol.* **2023**, *460*, 129423.

[5] Yasakau, K. A.; Kallip, S.; Zheludkevich, M. L.; Ferreira, M. G. S. Active corrosion protection of AA2024 by sol–gel coatings with cerium molybdate nanowires. *Electrochim. Acta* **2013**, *112*, 236–246.

[6] Abrantes Leal, D.; Wypych, F.; Bruno Marino, C. E. Zinc-layered hydroxide salt intercalated with molybdate anions as a new smart nanocontainer for active corrosion protection of carbon steel. *ACS Appl. Mater. Interfaces* **2020**, *12*, 19823–19833.

[7] Wang, T. G.; Cao, H. J. Orientation control and characterization strategies towards developing 2D materials-based composite coatings for corrosion protection on metals: Progresses and challenges. *Prog. Org. Coat.* **2023**, *182*, 107715.

[8] Wang, J. B.; Zhao, J. M.; Tabish, M.; Shi, F.; Fan, B. M.; Peng, L. J.; Cheng, Q. Intelligent anticorrosion coating based on mesostructured BTA@mCeO_2/g-C_3N_4 nanocomposites for inhibiting the filiform corrosion of Zn-Mg-Al coated steel. *Corros. Sci.* **2023**, *221*, 111331.

[9] Liu, W.; Yu, J. G.; Li, T. S.; Li, S. H.; Ding, B. Y.; Guo, X. L.; Cao, A. Q.; Sha, Q. H.; Zhou, D. J.; Kuang, Y. et al. Self-protecting CoFeAl-layered double hydroxides enable stable and efficient brine oxidation at 2 A·cm^{-2}. *Nat. Commun.* **2024**, *15*, 4712.

[10] Zhang, Y.; Feng, B.; Yan, M. L.; Shen, Z.; Chen, Y. Q.; Tian, J. Y.; Xu, F. F.; Chen, G. H.; Wang, X. Z.; Yang, L. J. et al. Self-supported NiFe-LDH nanosheets on NiMo-based nanorods as high-performance bifunctional electrocatalysts for overall water splitting at industrial-level current densities. *Nano Res.* **2024**, *17*, 3769–3776.

[11] Singha Roy, S.; Karmakar, A.; Madhu, R.; Nagappan, S.; N Dhandapani, H.; Kundu, S. Three-dimensional Sm-doped NiCu-LDH on Ni foam as a highly robust bifunctional electrocatalyst for total water splitting. *ACS Appl. Energy Mater.* **2023**, *6*, 8818–8829.

[12] Xing, X. T.; Sui, Y.; Li, Q. S.; Yuan, M.; Zhao, H. T.; Zhou, D.; Chu, X. M.; Liu, S. J.; Tang, E. J. Multifunctional ZnAl-MoO_4 LDH assembled $Ti_3C_2T_x$ MXene composite for active/passive corrosion protection behavior of epoxy coatings. *Appl. Surf. Sci.* **2023**, *623*, 157092.

[13] Yasakau, K. A.; Kuznetsova, A.; Maltanava, H. M.; Poznyak, S. K.; Ferreira, M. G. S.; Zheludkevich, M. L. Corrosion protection of zinc by LDH conversion coatings. *Corros. Sci.* **2024**, *229*, 111889.

[14] Karthik Kiran, S.; Shukla, S.; Struck, A.; Saxena, S. Surface engineering of graphene oxide shells using lamellar LDH nanostructures. *ACS Appl. Mater. Interfaces* **2019**, *11*, 20232–20240.

[15] Ahmad, E. A.; Chang, H. Y.; Al-Kindi, M.; Joshi, G. R.; Cooper, K.; Lindsay, R.; Harrison, N. M. Corrosion protection through naturally occurring films: New insights from iron carbonate. *ACS Appl. Mater. Interfaces* **2019**, *11*, 33435–33441.

[16] Xiong, Z. Z.; Qi, Z. H.; Zhang, W. H.; Ji, M. B.; Ma, F. Q.; Ying, L. X.; Wang, G. X. Enhancing frictional and corrosion resistance performance in aluminum alloy through *in situ* growth of NiZnAl-LDH membrane and its modification. *Surf. Interfaces* **2024**, *46*, 104103.

[17] Yashas, S. R.; Shivaraju, H. P.; Sandeep, S.; Kumara Swamy, N.; Gurupadayya, B. Application of yttrium molybdate tethered polypyrrole nanocomposite for the photocatalytic remediation of nitrofurantoin in water. *Surf. Interfaces* **2022**, *32*, 102102.

[18] Chen, Y. X.; Zhou, D.; Guo, X. J.; Yang, X.; Zhao, S. R.; Lu, Y.; Liu, J. K. Improved anticorrosion performance of mixed valence Mn-modified ZnO dilute magnetic solid solution with multilevel self-assembled network structure. *Nano Res.* **2022**, *15*, 6590–6600.

[19] Mu, X. Q.; Zhang, X. Y.; Chen, Z. Y.; Gao, Y.; Yu, M.; Chen, D.; Pan, H. Z.; Liu, S. L.; Wang, D. S.; Mu, S. C. Constructing symmetry-

mismatched $Ru_xFe_{3-x}O_4$ heterointerface-supported Ru clusters for efficient hydrogen evolution and oxidation reactions. *Nano Lett.* **2024**, *24*, 1015–1023.

[20] Wang, S. C.; Zhang, M. Y.; Mu, X. Q.; Liu, S. L.; Wang, D. S.; Dai, Z. H. Atomically dispersed multi-site catalysts: Bifunctional oxygen electrocatalysts boost flexible zinc-air battery performance. *Energy Environ. Sci.* **2024**, *17*, 4847–4870.

[21] Liu, Y.; Yao, H.; Xie, Z. H.; Yu, G.; Zhong, C. J. *In situ* depositing a metal-organic framework film on TiO_2 nanoarray toward stable photogenerated cathodic protection for nickel-coated magnesium alloy. *Appl. Surf. Sci.* **2023**, *638*, 157937.

[22] Guo, Y.; Jiang, Z. Q.; Ying, W.; Chen, L. P.; Liu, Y. Z.; Wang, X. B.; Jiang, Z. J.; Chen, B. L.; Peng, X. S. A DNA-threaded ZIF-8 membrane with high proton conductivity and low methanol permeability. *Adv. Mater.* **2018**, *30*, 1705155.

[23] Man, T. T.; Xu, C. X.; Liu, X. Y.; Li, D.; Tsung, C. K.; Pei, H.; Wan, Y.; Li, L. Hierarchically encapsulating enzymes with multi-shelled metal-organic frameworks for tandem biocatalytic reactions. *Nat. Commun.* **2022**, *13*, 305.

[24] Duan, P. F.; An, Y. H.; Wei, X. X.; Tian, Y. J.; Guan, D.; Liu, X. W.; Mao, L. Q. A novel structure of ultra-high-loading small molecules-encapsulated ZIF-8 colloid particles. *Nano Res.* **2024**, *17*, 2929–2940.

[25] Chen, F. J.; Mu, X. Q.; Zhou, J. L.; Wang, S. C.; Liu, Z. Y.; Zhou, D. Y.; Liu, S. L.; Wang, D. S.; Dai, Z. H. Engineering the active sites of MOF-derived catalysts: From oxygen activation to activate metal-air batteries. *Chin. J. Chem*., in press, DOI: 10.1002/cjoc.202400332.

[26] Huang, Y.; Zhao, C. Y.; Li, Y.; Wang, C.; Yuan, W. L.; Shen, T.; Liu, J.; Cheng, D.; Wu, C. C.; Shen, Q. H. et al. A smart sol–gel coating incorporating pH-responsive BTA-ZIF-8 MOF assembled hexagonal boron nitride for active/passive corrosion protection of 1060 aluminum alloy. *Surf. Coat. Technol.* **2023**, *474*, 130072.

[27] Zhong, Y.; Wu, C. L.; Jia, X. F.; Sun, S. J.; Chen, D. M.; Yao, W. Q.; Ding, H.; Zhang, J. Y.; Ma, T. Y. Coupling of self-healing atomic layer CoAl-LDH onto Mo:$BiVO_4$ photoanode for fast surface charge transfer toward stable and high-performance water splitting. *Chem. Eng. J.* **2023**, *465*, 142893.

[28] Fu, M. J.; Chai, B.; Zhang, X. H.; Sun, Y.; Fan, G. Z.; Song, G. S. Nitrogen self-doped chitosan carbon aerogel integrating with CoAl-LDH for ultra-efficient sulfamethoxazole degradation based on PS-AOPs: From batch to continuous process. *J. Environ. Chem. Eng.* **2023**, *11*, 110650.

[29] Xu, J.; Li, Q.; Liu, X. Y.; Yang, Q. P-doped nanorod MoO_3 and nanoflower NiAl-LDH construct S-type heterojunction for photocatalytic high-efficiency hydrogen evolution. *Surf. Interfaces* **2023**, *43*, 103593.

[30] Li, Z. K.; Xu, Z. H.; Wang, G. S.; Ding, Y. J.; Yan, Z. X.; Yue, L. Interfacial construction promoted binder-free NiCo-LDH/Mn-ZIF on carbon cloth for high-performance supercapacitor. *Electrochim. Acta* **2024**, *475*, 143701.

[31] Zhang, Y. Y.; Liu, H.; Zhu, P. F.; Yang, M. X.; Jin, Z. L. *In situ* XPS proved effective charge transfer over ZIF-67@CoFe LDH S-scheme heterojunctions for efficient visible light driven hydrogen evolution. *Int. J. Hydrogen Energy* **2023**, *48*, 32631–32641.

[32] Wang, G. R.; Jin, Z. L.; Zhang, W. X. Ostensibly phosphatized NiAl LDHs nanoflowers with remarkable charge storage property for asymmetric supercapacitors. *J. Colloid Interface Sci.* **2020**, *577*, 115–126.

[33] Tonda, S.; Kumar, S.; Bhardwaj, M.; Yadav, P.; Ogale, S. g-C_3N_4/NiAl-LDH 2D/2D hybrid heterojunction for high-performance photocatalytic reduction of CO_2 into renewable fuels. *ACS Appl. Mater. Interfaces* **2018**, *10*, 2667–2678.

[34] Sun, C.; Hu, J.; Wu, L. X.; Xia, Q. L.; Jiao, F. P. Construction of a novel visible-light-driven Z-scheme NiAl-LDH modified $(BiO)_2CO_3$ heterostructure for enhanced photocatalytic degradation antibiotics performance in natural water bodies. *Ind. Eng. Chem. Res.* **2023**, *62*, 466–477.

[35] Liu, Q.; Zhou, F.; Bai, Y. Y.; Hu, W. K. Evaluating properties of carbon-free nano-NiCoFe-LDHs with molybdate as oxygen evolution catalysts and their applications in rechargeable air electrodes. *Energy Fuels* **2021**, *35*, 20374–20385.

[36] Wang, H. O.; Wang, H. M.; Wang, H. F.; Su, Q. D.; Jiang, H.; Pan, Y. P.; Ma, X. F.; Hao, S. J.; Liu, J. W. β supported $Fe_2(MoO_4)_3$: An efficient solid acidic heterogeneous catalyst for the synthesis of 2-ethoxyethyl acetate. *Microporous Mesoporous Mater.* **2024**, *369*, 112985.

[37] Popov, V. V.; Menushenkov, A. P.; Yastrebtsev, A. A.; Molokova, A. Y.; Rudakov, S. G.; Svetogorov, R. D.; Tsarenko, N. A.; Ponkratov, K. V.; Ognevskaya, N. V.; Seregina, O. N. The effect of the synthesis conditions on the structure and phase transitions in $Ln_2(MoO_4)_3$. *Solid State Sci.* **2021**, *112*, 106518.

[38] Chen, X.; Fan, B. C.; Wang, H.; Liu, X. F.; Liu, Y.; Gao, J. K. Multiflower-like ReS_2/NiAl-LDH heterojunction for visible-light-driven photocatalytic CO_2 reduction. *Inorg. Chem.* **2024**, *63*, 5132–5141.

[39] Kalusulingam, R.; Mariyaselvakumar, M.; Antonyraj, C. A.; Mathi, S.; Mikhailova, T. S.; Khubezhov, S. A.; Pankov, I. V.; Srinivasan, K.; Myasoedova, T. N. Highly efficient water splitting with Pd-integrated NiAl-LDH nanosheets as bifunctional electrocatalysts. *Energy Fuels* **2023**, *37*, 13319–13330.

[40] Chaudhary, K.; Dhiman, D.; Venkatesu, P.; Masram, D. T. Classically synthesized ZIF-8 and Au/ZIF-8 for biocompatibility assessment with hemoglobin. *ACS Sustain. Chem. Eng.* **2022**, *10*, 12962–12967.

[41] Wang, X. B.; Liu, J.; Leong, S.; Lin, X. C.; Wei, J.; Kong, B.; Xu, Y. F.; Low, Z. X.; Yao, J. F.; Wang, H. T. Rapid construction of ZnO@ZIF-8 heterostructures with size-selective photocatalysis properties. *ACS Appl. Mater. Interfaces* **2016**, *8*, 9080–9087.

[42] Pei, X. Y.; Song, W. Y.; Zhang, Z. W.; Zhao, Y.; Li, Z. Y. CO_2-responsive CuI-ionic liquid/zeolitic imidazolate frameworks stabilized Pickering emulsions for azide-alkyne click reaction. *ACS Appl. Nano Mater.* **2023**, *6*, 19972–19980.

[43] Ding, R. J.; Zhu, H. F.; Zhou, J. S.; Luo, H. H.; Xue, K. H.; Yu, L. Q.; Zhang, Y. P. Highly water-stable and efficient hydrogen-producing heterostructure synthesized from $Mn_{0.5}Cd_{0.5}S$ and a zeolitic imidazolate framework ZIF-8 via ligand and cation exchange. *ACS Appl. Mater. Interfaces* **2023**, *15*, 36477–36488.

[44] Niu, X. H.; Yan, S. M.; Zhao, R.; Li, H. X.; Liu, X. Y.; Wang, K. J. Design and electrochemical chiral sensing of the robust sandwich chiral composite D-His-ZIF-8@Au@ZIF-8. *ACS Appl. Mater. Interfaces* **2023**, *15*, 22435–22444.

[45] Mu, C. L.; Ren, J. H.; Chen, H.; Wu, Y.; Xu, Q. N.; Sun, X. D.; Yan, K. Graphitic carbon nitride/zeolitic imidazolate framework-8 nanoparticles with antibacterial properties for textile coating. *ACS Appl. Nano Mater.* **2021**, *4*, 10634–10644.

[46] Jin, Z. L.; Wang, X. Y.; Wang, Y. P.; Yan, T.; Hao, X. Q. Snowflake-like Cu_2S coated with NiAl-LDH forms a p–n heterojunction for efficient photocatalytic hydrogen evolution. *ACS Appl. Energy Mater.* **2021**, *4*, 14220–14231.

[47] Ma, B. C.; Zhang, C.; Jia, D. J.; Zhao, Q. X.; Yang, P. P. NiAl-LDH-modified core–shell rod-like ZnO@ZnS heterostructures for enhanced photocatalytic hydrogen precipitation. *J. Phys. Chem. C* **2023**, *127*, 2908–2917.

[48] Ren, R.; Liu, G. C.; Kim, J. Y.; Ardhi, R. E. A.; Tran, M. X.; Yang, W.; Lee, J. K. Photoactive g-C_3N_4/CuZIF-67 bifunctional electrocatalyst with staggered p–n heterojunction for rechargeable Zn-air batteries. *Appl. Catal. B: Environ.* **2022**, *306*, 121096.

[49] Tantisriyanurak, S.; Klinyod, S.; Leangsiri, W.; Nunthakitgoson, W.;

Soyphet, A.; Ketkaew, M.; Thivasasith, A.; Iadrat, P.; Rodaum, C.; Atithep, T. et al. Carbon nanotubes deposited on mordenite zeolite/NiAl-layered double hydroxide composites as electrocatalysts for 2,5-furandicarboxylic acid production from 5-hydroxymethylfurfural. *ACS Appl. Nano Mater.* **2023**, *6*, 8784–8794.

[50] Wu, Y. L.; Zhu, P. F.; Li, Y. J.; Zhang, L. J.; Jin, Z. L. *In situ* derivatization of NiAl-LDH/NiS a p–n heterojunction for efficient photocatalytic hydrogen evolution. *ACS Appl. Energy Mater.* **2022**, *5*, 8157–8168.

[51] Ma, X. L.; Zhou, L. X.; Chen, T.; Sun, P. P.; Lv, X. W.; Yu, H. Z.; Sun, X. H.; Leo Liu, T. High-performance aqueous rechargeable NiCo//Zn battery with molybdate anion intercalated CoNi-LDH@CP bilayered cathode. *J. Colloid Interface Sci.* **2024**, *658*, 728–738.

[52] Ju, X. Q.; Yang, Z. Y.; Wang, J. W.; Cui, B. L.; Xin, Y. Y.; Zheng, Y. P.; Wang, D. C. Converting nanoflower-like layered double hydroxides into solvent-free nanofluids for CO_2 capture. *ACS Appl. Mater. Interfaces* **2023**, *15*, 56181–56191.

[53] Wang, Q. X.; Lei, Y. T.; Cui, Y. Y.; Lin, J. R. L.; Huang, W.; He, Y. Thermal stability and kinetics of single I_2@ZIF-8 particles. *ACS Appl. Mater. Interfaces* **2022**, *14*, 22643–22649.

[54] Tian, J. J.; Chen, Y. X.; Liu, Z. X.; Liu, J. K. Synthesis and mechanism of Co^{2+}/Sr^{2+} codoped magnetic lanthanum cuprate with excellent corrosion resistance. *ACS Appl. Mater. Interfaces* **2023**, *15*, 53651–53664.

[55] Liu, S. Y.; Duan, J. Q.; Zhang, M. Y.; Wang, H.; Liu, Y. X.; Chen, W. P.; Wen, H. M.; Fu, Z. Q. Correlation of microstructure, mechanical properties and corrosion behavior in a $Ni_{34}Co_{28}Cr_{28}Al_{10}$ multi-principal element alloy with outstanding corrosion resistance. *Corros. Sci.* **2024**, *228*, 111835.

[56] Liu, Z. X.; Zhou, D.; Tian, J. J.; Liu, J. K. Vanadium-doped induction of bare active crystalline planes of tungsten oxide and its excellent anticorrosion properties. *ACS Appl. Eng. Mater* **2023**, *1*, 2926–2940.

[57] Wang, Z.; Jin, Z. Y.; Liu, H. X.; Liu, R. L.; Zhang, Y.; Yin, Y. S.; Liu, H. F.; Yuan, X.; Fan, S. J.; Liu, H. W. Insights into the hydrophobic coating with integrated high-efficiency anti-corrosion, anti-biofouling and self-healing properties based on anti-bacterial nano LDH materials. *Corros. Sci.* **2024**, *231*, 111995.

[58] Zan, G. T.; Li, S. Q.; Chen, P.; Dong, K. Z.; Wu, Q. S.; Wu, T. Mesoporous cubic nanocages assembled by coupled monolayers with 100% theoretical capacity and robust cycling. *ACS Cent. Sci.* **2024**, *10*, 1283–1294.

[59] Song, L. Y.; Ma, X. M.; Chen, Z. Y.; Hou, B. R. The role of UV illumination on the initial atmospheric corrosion of 09CuPCrNi weathering steel in the presence of NaCl particles. *Corros. Sci.* **2014**, *87*, 427–437.

[60] Xu, D.; Zhang, S. N.; Chen, J. S.; Li, X. H. Design of the synergistic rectifying interfaces in Mott–Schottky catalysts. *Chem. Rev.* **2023**, *123*, 1–30.

[61] Yamasaki, T.; Iimura, S.; Kim, J.; Hosono, H. Extremely shallow valence band in lanthanum trihydride. *J. Am. Chem. Soc.* **2023**, *145*, 560–566.